 doi:10.20944/preprints202005.0434.v1

33rd Symposium on Naval Hydrodynamics
Osaka, Japan, 18 October-23 October 2020

Augmenting Maneuverability of UUVs with Cycloidal Propellers

Manavendra Desai[1], Ruddhi Gokhale[1], Atanu Halder[2], Moble Benedict[2], Yin Lu Young[1,3]

([1]Department of Mechanical Engineering, The University of Michigan Ann Arbor, United States, [2]Advanced Vertical Flight Laboratory, Texas A&M University, United States,[3] Department of Naval Architecture and Marine Engineering, The University of Michigan, Ann Arbor, United States)

ABSTRACT

This paper investigates the novel concept of augmenting the maneuverability of underwater vehicles with cycloidal propellers. Cycloidal propellers have the potential of providing agile manoeuvring capabilities to an underwater vehicle such as enabling pure heave motion and spot turns. They will also enable the vehicle to surge in forward and backward directions with equal ease. Such manoeuvres are not possible with the more conventional screw propeller and control fin combinations. Moreover, cycloidal propellers can enable precise dynamic positioning in low speed applications like station-keeping, underwater surveying and maintenance, minesweeping and teaming activities. In this paper, manoeuvring capabilities of an underwater vehicle with conventional screw propeller and control fins only are compared with one augmented with cycloidal propellers. The cases considered include a turning circle manoeuvre, a low speed 180^o turn and a low speed heave manoeuvre. A six degrees-of-freedom non-linear hydrodynamic motion prediction model was developed and validated. Simulation results demonstrated that compared to conventional propulsion systems, cycloidal propeller augmented underwater vehicles can be more swift and compact in low speed manoeuvres, making a case for further investigation into this concept.

1. INTRODUCTION

Unmanned underwater vehicles (UUVs) are widely utilized by defense, educational and commercial institutions for operations such as oceanic exploratory surveys and environment monitoring, maintenance of offshore renewable energy farms, pipeline inspections and minesweeping (Griffiths, 2002). Using on-board data acquisition systems, UUVs help us tap into and efficiently navigate precarious waters without risking lives of human operators.

During a mission, marine life, seamounts and debris are few of the obstacles a UUV may encounter while operating in confined spaces. Waves and currents are unwanted disturbances which a UUV may also be subjected to. Adding to the challenge is the inherent bandwidth limitation of underwater communication systems. GPS fixes and acoustic links are the most common interaction techniques (Nicholson and Healey, 2008) but are used only a limited number of times over the course of a mission. This reduced opportunity to communicate with the vehicle points us towards the need for enhanced UUV autonomy, especially when travelling in restricted waters (Griffiths, 2002). Providing swift, compact and agile maneuvering will facilitate UUV autonomy and teaming activities, which will contribute to their performance and function in challenging waters. Such a form of enhanced autonomy can also be extended to achieve superior station-keeping, sea-keeping and coordinated maneuvers for military applications and also develop more effective autonomous search and rescue vehicles.

At the present, most UUVs are thrusted and steered using screw propellers (SP)/Kort nozzles and control surfaces (fins) such as rudders and elevators. Since a control surface generates steering forces proportional to square of the inflow velocity, at low UUV speeds, they are bound to be less effective and the UUV will respond sluggishly. This does not auger well for operations such as inspection, imaging and station-keeping, which are carried out at low speeds and require

Preprints (www.preprints.org) | NOT PEER-REVIEWED | Posted: 26 May 2020 doi:10.20944/preprints202005.0434.v1

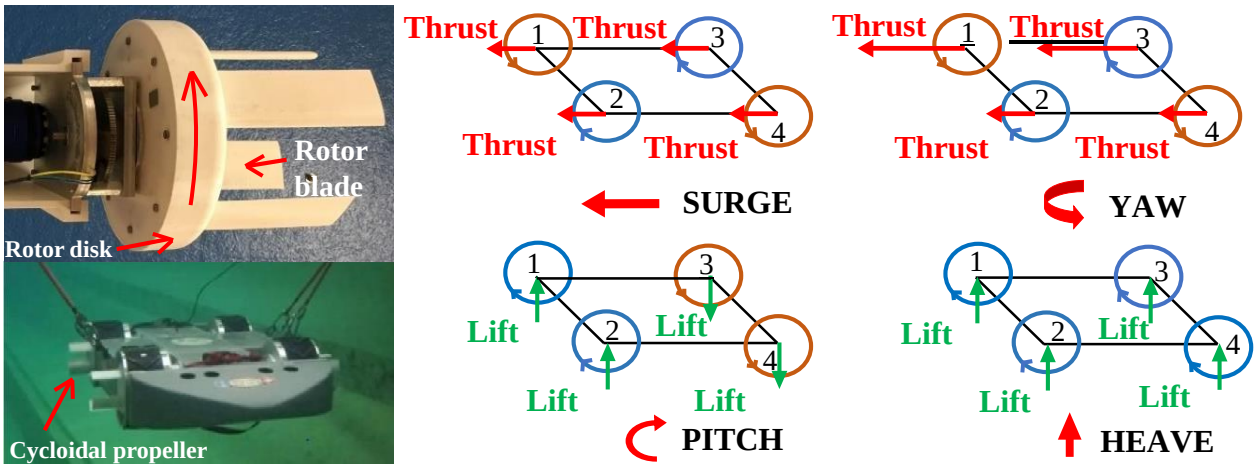

Figure 1: On the top left is a cycloidal propeller designed and manufactured in the Advanced Vertical Flight Laboratory at Texas A&M University. It was built for a reduced scale amphibious platform, seen here on the bottom left in a towing tank test, developed as part of a collaborative project between Texas A&M University and the University of Michigan-Ann Arbor. The amphibious vehicle is thrusted *and* maneuvered solely by these cycloidal propellers. Reasonable control was observed up to model speeds of 0.15 m/s. A conceptual configuration for a cycloidal propeller *driven* UUV is shown on the right, wherein the UUV represented by parallelograms in black - is driven by four cycloidal propellers - represented by the blue and brown circles. Their axis of rotation lies in the same horizontal plane as the UUV . The arrows on the circles give the direction of rotation of the respective cycloidal propeller rotor disks. Components of thrust and lift are given by red and green arrows wherein a larger arrow depicts a larger maneuvering force. A cycloidal propeller rotating forward (in the direction of surge) produces a downward lift force while a cycloidal propeller rotating backwards produces an upward lift. Thrust is always directed forward. For surge and yaw, the cycloidal propeller force is purely in thrust form while for pitch and heave it is purely in lift form. 360º thrust vectoring such as this will allow the UUV to move in all the six degrees of freedom using the same set of four cycloidal propellers, without the need of additional propulsors, thrusters or control surfaces.

high UUV controllability for precise maneuvering. In general, fins are effective at speeds above 3 knots, while tunnel/ducted thrusters are the common *additional* propulsors necessary to compliment fins and aid maneuvering at speeds below 1.5 knots (Cancilliere, 1994).

Apart from speed, the flow regime in which a UUV operates also affects the propeller and fin performance. At low speeds and low Reynolds numbers, it is challenging to keep a steady flow attached over a fin, limiting its range of angle of attack and effectively its deflection, beyond which flow separation and stall will occur. Fins and propeller blades suffer a similar fate in unsteady and turbulent flows experienced commonly in shallow water, waves and swells, resulting in an inability to station-keep and maneuver precisely.

Water jets/pump jets are possible alternatives. Their movable nozzles vector thrust to steer vehicles, hence eliminating dependence on fins and also yielding the capability to turn on the spot. However, due to their hull piercing ducts, they will always cause loss of usable volume and buoyancy as well as increase frictional drag. At low UUV speeds (<1.5 knots), water flow-rates into the pump will be low, reducing thrust coefficients and operating efficiencies of the water jet as a whole. The shortcomings discussed heretofore can be overcome by employing a class of cross-flow propellers called *cycloidal* propellers.

Cycloidal propellers (CP) work on the principle of a fish's fin, in that they utilize unsteady hydrodynamics and leading-edge vortices to generate thrust (Halder et al., 2017) and provide maneuverability in multiple degrees of freedom (DOF). As can be seen in Figure 1, the blade spans parallel to the axis of rotation and a rotor disk creates the flow velocity required by the blades to produce necessary maneuvering forces. By altering rotor speeds and rotor blade angles, CP provide 360º thrust vectoring capability in the surge-sway-yaw plane to a surface vehicle. On the other hand, as can be seen in Figure 1, a CP steered UUV can also alter depth by moving straight up or down. Such features of CP can eliminate dependence on control surfaces like rudders and elevators. The addition of CP can allow compact maneuvering in addition to allowing more degrees of freedom, be it at low speeds or in turbulent and unsteady flow regimes. Figure 1 also shows a proof-of-concept test of a CP thrusted and maneuvered amphibious vehicle, tested at The Aaron Friedman Marine Hydrodynamics Laboratory at the University of

Preprints (www.preprints.org) | NOT PEER-REVIEWED | Posted: 26 May 2020 doi:10.20944/preprints202005.0434.v1

Michigan. During the test, reasonable control was achieved up to speeds of 0.15 m/s, showing that the concept of a CP maneuvered UUV can be a viable one. CP have already been successfully implemented in micro-aerial vehicles (MAV) (Benedict et al., 2013a; Halder & Benedict, 2018), where a small size, low weight and low air resistance meant the thrust produced by CP was sufficiently high to provide both propulsion *and* control.

Incorporating CP in a UUV is an involved process because of the large and destabilizing hydrodynamic loads experienced in water (where the fluid density is ~ 850 times higher than air). Free surface effects, waves, ventilation and possibility of rotor blades cavitating at high rotation speeds will only add to the complexity. Also well known is that compared to other propulsors, CP consume higher power and hence must preferably be used at low UUV and low CP rotation speeds (power consumed $\propto$ propeller speed^3). Therefore, the objective of the present work is to investigate maneuvering characteristics of a CP *augmented* UUV and compare it with that of an SP-control fin driven UUV. The CP augmented UUV concept has CP in addition to an SP and control fins. The CP will thrust and maneuver the UUV at low speeds and will be used to augment the thrust and maneuverability of the SP-control fin combination at higher speeds. To this end, a reduced order maneuvering model (ROM) and MATLAB (The MathWorks, Inc) code was developed and validated. Quicker and computationally cheaper than traditional CFD methods, it solves a 6-DOF non-linear coupled equation of motion to predict UUV trajectory. Being a ROM, it will also allow easier interfacing with controller design software for future simulations and experiments.

NOMENCLATURE

Cycloidal propeller

α	Inflow angle at rotor blade
α_{eff}	Effective angle of attack at rotor blade
α_i	Induced angle of attack at rotor blade
β	Rotor disk azimuthal angle
Γ	Circulation due to lift at rotor blade
γ	Rotor disk phase angle
λ	Advance coefficient
ω	Rotor disk angular velocity
ρ	Fluid density
θ	Rotor blade geometric angle of attack
b	Rotor blade span
c	Rotor blade chord
C_L	Total lift coefficient of rotor blade
$C_{L\alpha}$	Lift - angle of attack curve slope for rotor blade
C_{Lo}	Lift coefficient of rotor blade due to virtual camber effect
d	Rotor disk diameter
N	Cycloidal propeller rotations per minute
S_{blade}	Rotor blade planform area
u	Rotor blade peripheral velocity
V	Net inflow velocity at rotor blade
V_b	Inflow velocity due to curvilinear flow along blade orbit
V_i	Inflow velocity due to other rotor blades
V_p	Inflow velocity due to rotor blade pitching
V_∞	Free-stream velocity
x	Abscissa in rotor blade coordinate system
y	Span-wise location along rotor blade
η	Open water efficiency
Ω	UUV rotational velocity
C	Total UUV Coriolis-centripetal matrix
C_A	UUV added-mass Coriolis-centripetal matrix
C_S	UUV Coriolis-centripetal matrix
C_T	Required thrust coefficient
$C_{D,fin}$	Control fin drag coefficient
$C_{L,fin}$	Control fin lift coefficient
D	Total UUV damping matrix
D_l	Linear damping matrix
D_{fin}	Control fin generated drag
D_{nl}	Non-linear damping matrix
F_{fin}	UUV control fin generated forces
$g_{(\Delta)}$	UUV hydrostatic stiffness matrix

UUV Dynamics

g_o	UUV self-weight
K_Q	Torque coefficient
K_T	Obtained thrust coefficient
l	UUV propeller thrust line vector
L_{fin}	Control fin generated lift
M	Total UUV mass matrix
M_A	UUV added-mass mass matrix
M_p	UUV propeller thrust induced moment
M_S	UUV structural mass matrix
M_{fin}	UUV control fin generated moments
Q	UUV propeller reaction torque on hull
r_{hc}	Position vector of hydrodynamic center of control fins
S_{fin}	Planform area of control fins
T	UUV propeller thrust
T_p	UUV propeller forces and moments
U	UUV translational velocity
$V_{\infty,hc}$	Net inflow velocity at control fin hydrodynamic center

Preprints (www.preprints.org) | NOT PEER-REVIEWED | Posted: 26 May 2020 doi:10.20944/preprints202005.0434.v1

2. MATERIALS AND METHODS

2.1 Cycloidal Propellers

The primary advantage that CP provide to a marine craft is high maneuverability through 360^o thrust vectoring. They are *cycloidal* in the sense that these cross-flow propellers are *low pitch* propellers, that is, they are designed to operate at an advance coefficient $\lambda < 1$ (Roesler et al., 2014) where $\lambda = V_\infty / u$. V_∞ is the free-stream velocity in the frame of the propeller, while $u = \omega R = \pi n D$ is the rotor blade peripheral velocity.

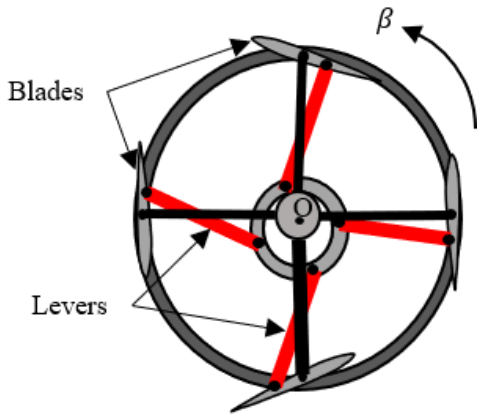

Figure 2: Simplified construction of a cycloidal propeller with pitching levers and four blades. The four levers project from an annular *control* ring as shown. This control ring is moved in the plane of the paper to alter the blade pitch amplitude θ_{max} and propeller phase angle γ in order to vector thrust.

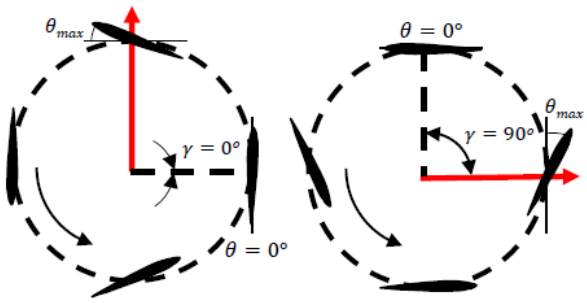

Figure 3: A cycloidal propeller rotor blade at a phase of γ = 0^o and γ = 90^o. θ_{max} is the rotor blade pitch amplitude while the red arrows indicate direction of the net propeller force. The cycloidal propeller is experiencing no external inflow and is rotating in the anticlockwise direction. As can be seen, at γ = 0^o the entire propeller force is in the form of lift, while at γ = 90^o it is in the form of thrust. Phase increment is considered positive in the clockwise direction for the given configuration.

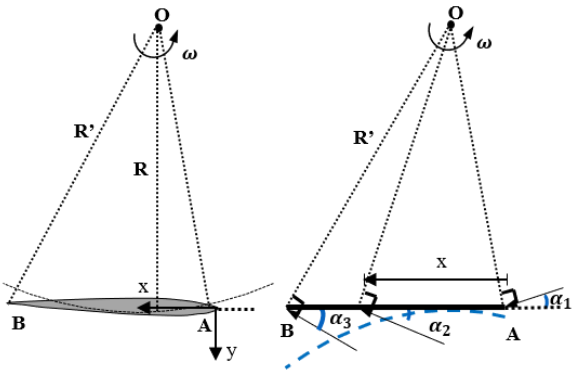

Figure 4: A cycloidal propeller rotor blade rotating about its axis O with angular velocity ω along a curvature of radius R. The angle of attack α varies along the chord due to changing curvilinear velocity, inducing a *virtual* camber in an otherwise symmetrical hydrofoil. This virtual camber is shown by the dashed blue line on the right.

Figure 2 shows a simplified schematic of the CP mechanism. As the rotor disk rotates an azimuthal angle β about its pivot O, side levers pitch the rotor blades by an angle θ about their respective pivots O. This results in a dynamically varying pitch angle along the azimuth for each blade. For every single rotation of the rotor disk, the rotor blade will oscillate one cycle. The oscillation kinematics of the blades can be sinusoidal or cycloidal. Each blade pitching lever is actuated by a *control* ring which can change the azimuth angle from where the rotor blades begin pitching (θ = 0^o) about their pivots. This azimuth angle is called the phase angle γ of the cycloidal propeller (Figure 3). γ and the CP rotation speed ω are the two controllable parameters which can vector CP thrust according to a given maneuvering command. Blade pitching angle θ is commonly associated with the rotor disk position β in either of the following two ways (Roesler et al., 2016),

$$\theta_{sinusoidal} = a\sin(\beta + \gamma) \quad (1)$$

$$\theta_{cycloidal} = a\tan^{-1}\left(\frac{e\sin\beta}{1+e\cos\beta}\right) \quad (2)$$

a is the blade pitch amplitude while e (<1) is the eccentricity of cycloidal blade motion. Eq. 1 and 2 provide blade pitch kinematics for sinusoidal and cycloidal pitching respectively. This work uses cycloidal formula (Eq. 2) for pitch angle.

Figure 4 throws light on the inflow experienced by a CP rotor blade as it moves along the azimuth. A

Preprints (www.preprints.org) | NOT PEER-REVIEWED | Posted: 26 May 2020 doi:10.20944/preprints202005.0434.v1

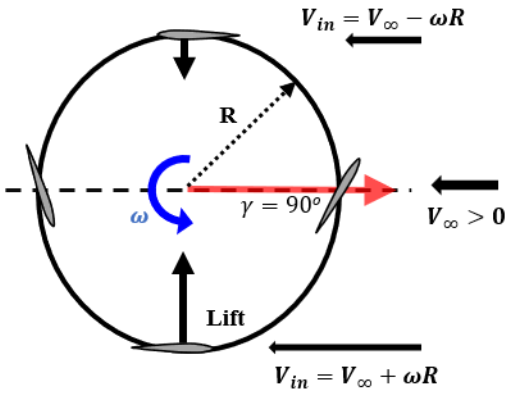

Figure 5: A non-zero free-stream velocity V_∞ causes different relative horizontal inflow V_{in} at the top and bottom rotor blades, leading to a non-zero lift even at a phase angle γ = 90^o. ω is the rotation speed of the cycloidal propeller while R is the radius of the rotor blade orbit. In this configuration, the net hydrodynamic force will be tilted upwards.

symmetrical hydrofoil moving on a curvilinear path experiences a varying angle of attack along its chord. This is because when the rotor blade rotates about *O*, at a given azimuth angle β, the inflow velocity angle varies gradually from α_1 at the leading edge *A* to α_3 at the trailing edge *B*. To add to this is the varying blade pitch angle θ. This generates a *virtual* camber which is a function of the distance from leading edge *x* in the rotor blade coordinate system. Since the rotor blade also pitches about its pivot while the rotor disk rotates along the azimuth, the blade pitch θ and hence the inflow velocity at a given x is different at each azimuth position β on the rotor blade orbit. This leads to a *dynamic* virtual camber, meaning that the camber also varies with β and θ, in addition to being a function of *x*. Therefore, due to the dynamic virtual camber effect, a symmetrical hydrofoil moving on a curvilinear path can be modelled as a hydrofoil with a varying camber, as it moves on a rectilinear path.

The capability that allows a CP to instantaneously vector thrust is its phase changing ability. The phase angle γ of a CP is the angle along the azimuth at which the rotor blade starts pitching about its pivot. Hence, the blade pitch angle θ is 0^o when the rotor blade reaches an azimuth position β=γ. As can be seen in Figure 3, for a non-translating and purely rotating CP, at γ = 0^o, the net hydrodynamic force generated is expected to be vertically upwards because the rotor blade pitch angle θ is maximum at β=90^o and β=270^o azimuth angles, while the forces from rotor blades at β = 0^o and β= 180^o cancel out due to symmetry. Similarly, at γ = 90^o, the net hydrodynamic force is expected to be horizontally forward because θ is maximum at β = 0^o and β = 180^o azimuth angle, while the forces from rotor blades at β = 90^o and β = 270^o cancel out. However, this is not the case in practice. Previous experiments (Benedict et al., 2010) utilizing particle image velocimetry have shown that a non-zero transverse force will always exist under the above CP phase angles. It was observed that the wake shed downstream of the CP is skewed to one side and is thought to produce this transverse force. When employed on a UUV, this transverse force appears as lift (Figure 1). Here, for stable UUV motion in the surge-sway-yaw plane, one pair of diagonally located propellers (CP 1 and CP 4) are made to rotate opposite to the other pair of diagonally located propellers (CP2 and CP3) so as to cancel out the transverse lifts and moments generated. Likewise, CP can also be made to generate a direct forward or backward thrust which can enable the UUV to go forward and back with equal ease. In addition, all CP can be made to rotate in the same direction to generate an upward or downward thrust to heave up or down.

A rotating *and* translating CP however, has slightly different hydrodynamics. As can be seen in Figure 5, during forward motion at speed V_∞, there is difference in relative inflow velocities V_{in} at the top (90^o azimuth) and bottom (270^o azimuth) rotor blades of the propeller. Anti-clockwise rotation of the CP raises the inflow speed at the bottom rotor blade while it reduces the inflow velocity at the top rotor blade. As a result, the CP produces a differential lift force due to a greater upward lift at the bottom rotor blade than the downward lift at the top rotor blade. Blades L_1 and L_2 are therefore responsible for lift generation while blades T_1 and T_2 are responsible for thrust generation. T_2 generates most of the positive thrust force while T_1 usually generates a negative thrust (Halder & Benedict, 2018). Hence, unlike a purely rotating CP, a rotating and translating CP

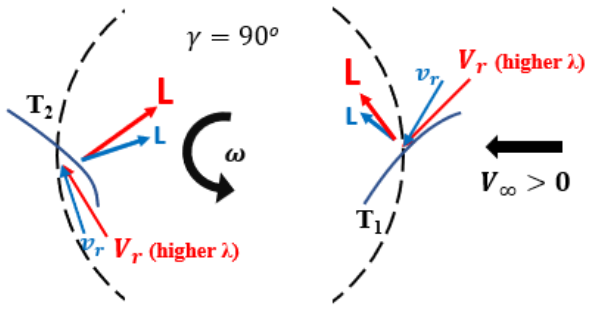

Figure 6: Effect of advance coefficient λ on thrust producing effectiveness of a cycloidal propeller. Higher lambda tends to orient rotor blade forces towards the vertical, increasing cycloidal propeller lift and reducing net thrust.

Preprints (www.preprints.org) | NOT PEER-REVIEWED | Posted: 26 May 2020 doi:10.20944/preprints202005.0434.v1

at a phase angle of $\gamma = 90^o$ will produce lift, at the cost of forward thrust. In such a case, phase γ will have to be increased further in the clockwise direction so as to reduce the lift to zero and increase CP thrust. With an increasing free-stream velocity V_∞, the required CP phase to produce pure thrust increases too. This is shown in Figure 6. Here, blades T_1 and T_2 are shown as their respective virtual cambers. As free-stream velocity V_∞ increases, for the same CP rotation speed, the advance coefficient λ increases too. The net inflow into the rotor blades is now more influenced by V_∞ than the circumferential (ωR) component, and hence tilts towards the horizontal. As a result, a higher net inflow V_r is incident at a lower effective angle of attack at the blades. This produces a rotor blade lift force L of larger magnitude, aligned more towards the vertical, which reduces the thrust producing capacity of the CP as a whole. Therefore, a cycloidal propeller at high advance coefficients will produce low thrust, which leads to low efficiency and high power consumption at high forward speeds. One possible countermeasure would be to increase the blade pitch amplitude.

A key geometrical aspect of the CP with regard to thrust producing capacity is the rotor blade chord c over rotor disk radius R ratio (Benedict et al., 2014). As the c/R ratio is increased, the virtual camber effect is increased due to a larger difference between angles of attacks of the circumferential flow velocity at the leading and trailing edges of the blade. An increased virtual camber reduces the effective angle of attack at the rotor blades and the CP starts producing more lift and less thrust. This would be feasible for lift production applications like hover in an air vehicle, but is not suitable for thrust production application in a UUV. One possible remedy is to increase R. This will reduce virtual camber effects along with the required CP rotation speed and drive down power requirements. However, care will have to be taken about the increasing rotor disk inertia since it will affect actuator design and associated power requirements. An alternative is to reduce the rotor blade chord length. This will also improve its hydrodynamic efficiency. However, care will have to be taken when increasing R or reducing c to ensure structural integrity.

Unsteady pitching of the CP blades discussed earlier creates leading edge vortices that delay stall and allow the blades to operate at higher angles of attack α (Shen and Fuhs, 1997). Also, blade-blade wake interaction tends to reduce the α at a blade and help delay stall. A reduced order aerodynamic model that takes into account such unsteady and virtual camber effects in a rotating CP has already been developed for micro-air vehicles (Halder and Benedict, 2018) and was used in the present study to simulate CP propulsive forces for the CP augmented UUV. A brief description of this model follows.

Mathematical Model - Since cycloidal propeller rotor blades both rotate along the azimuth and pitch about their pivots, co-ordinate transformations are needed to get the resultant inflow velocity $\boldsymbol{V}(x)$ in the frame of reference of the blade. $\boldsymbol{V}(x)$ will also be a function of the position x along the chord since the curvilinear flow produces a virtual camber in the hydrofoil. The geometry of a single blade can be seen in Figure 4.

$$\mathbf{V}(\mathbf{x}) = \mathbf{V_p}(\mathbf{x}) + \mathbf{V_i}(\mathbf{x}) + \mathbf{V}_\infty - \mathbf{V_b} \tag{3}$$

Here, $\boldsymbol{V}(x)$ is the resultant inflow velocity in the rotor blade frame of reference, $\boldsymbol{V_p}(x)$ is the linear velocity induced due to pitching motion of the blade, $\boldsymbol{V_i}(x)$ is the velocity induced due to other rotor blades, and $\boldsymbol{V_b}(x)$ is the velocity due to curvilinear flow in the rotor blade frame of reference. The final velocity $\boldsymbol{V}(x)$ can be decomposed into corresponding x and y components in the blade co-ordinate system as shown in Figure 4.

$$\mathbf{V}(\mathbf{x}) = -V_x\mathbf{i} + V_y\mathbf{j} \tag{4}$$

Using this formulation, the net inflow angle of attack $\alpha(x)$ in the rotor blade co-ordinate system can be determined as,

$$\alpha(x) = tan^{-1}\frac{V_y}{V_x} \tag{5}$$

Next, the coefficient of steady-state lift is determined using thin hydrofoil theory:

$$C_L = C_{L\alpha}\, sin(\alpha) + C_{Lo} \tag{6}$$

Here, C_{Lo} is the lift coefficient due to virtual camber effect. It is calculated by conformal mapping of the rotor blade co-ordinate system in a curvilinear flow onto a virtually cambered rotor blade co-ordinate system in rectilinear flow. The detailed process has been outlined in (Halder and Benedict, 2018). As already discussed earlier, pitching of the blades produces strong unsteady effects such as leading edge vortices and wake shedding. This is solved here and in (Halder and Benedict, 2018) using the Theodorsen's function and the Polhamus suction analogy. Upon computing the final rotor blade lift and drag coefficients, we obtain the lift and drag on one blade of the CP. For multiple blades at different azimuth positions, a stream tube model is used to calculate the total force generated by one cycloidal propeller. The modified double multiple stream tube model is used (Halder, A. Moble, 2018) to calculate the forces generated by one propeller with four rotor blades.

Preprints (www.preprints.org) | NOT PEER-REVIEWED | Posted: 26 May 2020 doi:10.20944/preprints202005.0434.v1

This CP model is validated with model experiments and is utilized in the six DOF maneuvering model as outlined next.

2.2. 6 DOF maneuvering model

A reduced order MATLAB computer code is used to solve a non-linear and coupled 6-DOF equation of motion for an underwater vehicle. Using forces and moments acting on the vehicle at one time step, the code calculates vehicle accelerations - in each DOF - at the next time step. These accelerations are then explicitly integrated in time to determine the vehicle's instantaneous trajectory and orientation. The framework behind this code is explained next.

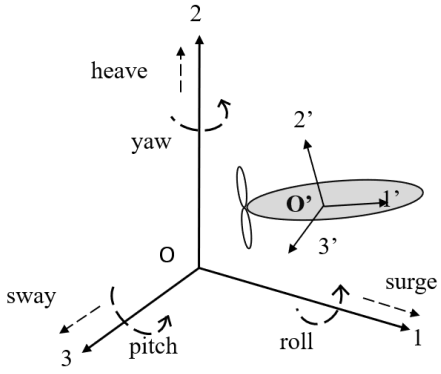

Figure 7: Figure 7: The coordinate systems used in formulating the equations of motion for the UUV. 1′2′3′ is the body fixed coordinate system while 123 is the inertial coordinate system.

Coordinate systems and Transformations - As shown in Figure 7, two coordinate systems are utilized in studying the vehicle motion, an inertial coordinate system *123* to track vehicle trajectory and a body fixed coordinate system *1'2'3'* to calculate propulsive, self-weight and hydrodynamic loads on the vehicle. Positive directions for motion in the six degrees of freedom are shown by the dotted arrows. At each time step during simulations, *1'2'3'* translates with the vehicle and assumes the same orientation as that of the vehicle, but does not rotate with it over the time step. Therefore, the vehicle will have a non-zero rotational velocity in this reference frame. *1'2'3'* has its origin at the located at the center of buoyancy (COB) of the vehicle.

The equation of motion is solved for vehicle accelerations and velocities in *1'2'3'*. These vectors are then oriented in *123* to solve for the vehicle trajectory. This is achieved using three principle rotations about the yaw (ψ), roll (ϕ) and pitch (θ) axes.

Mathematical Model - Eq. 8 gives the 6-DOF equation of motion used for the present study (Fossen, 2011; Hibbeler and Yap, 2012; Newman, 2018). It is assumed that the vehicle will operate in open water condition, i.e., at all times it is sufficiently far from the free surface, the seabed and any other solid boundary (Brennen, 1982).

$$\mathbf{M}\ddot{\mathbf{X}} + \mathbf{C}(\dot{\mathbf{X}})\dot{\mathbf{X}} + \mathbf{D}(\dot{\mathbf{X}})\dot{\mathbf{X}} + \mathbf{g}(\boldsymbol{\Delta}) + \mathbf{g_o} = \mathbf{T_p} \qquad (7)$$

$\boldsymbol{M} = \boldsymbol{M_S} + \boldsymbol{M_A}$ is the total (vehicle and fluid added) mass matrix while $\boldsymbol{C} = \boldsymbol{C_S} + \boldsymbol{C_A}$ is the total Coriolis centripetal matrix due to rotation of the vehicle and the fluid around it. $\boldsymbol{D} = \boldsymbol{D_l} + \boldsymbol{D_{nl}}$ is the combined linear (D_l) and non-linear (D_{nl}) damping matrix while $\boldsymbol{X} = [u, v, w, p, r, q]$ is the total velocity vector of the vehicle in 1'2'3'. Given the modelling assumptions made, D is purely viscous in nature and has no contributions from radiation damping or wave drag. However, the damping matrix incorporates all lift and drag forces and associated moments of the UUV hull and control fins for rotation and translation motion. $\boldsymbol{g}(\boldsymbol{\Delta})$ represents the buoyancy driven loads, where Δ is the vehicle displacement from its hydrostatic equilibrium position. $\boldsymbol{g_o}$ is the vehicle self-weight load and together with $\boldsymbol{g}_{(\Delta)}$ represents the hydrostatic forces and moments. On the right hand side is the applied propulsive forces and moments $\boldsymbol{T_p}$ that act on the vehicle. Expanded forms of these matrices with the required hydrodynamic derivatives are given in the appendix.

Numerical Model - To solve for $\boldsymbol{X}$ in time, the Coriolis centripetal, damping and hydrostatic loads are treated as applied forces and moments and taken to the right hand side as shown in Eq. 9.

$$\mathbf{M}\ddot{\mathbf{X}}_{\mathbf{n+1}} = -\mathbf{C}(\dot{\mathbf{X}}_{\mathbf{n}})\dot{\mathbf{X}}_{\mathbf{n}} - \mathbf{D}(\dot{\mathbf{X}}_{\mathbf{n}})\dot{\mathbf{X}}_{\mathbf{n}} - \mathbf{g}(\boldsymbol{\Delta}_{\mathbf{n}}) - \mathbf{g}_{\mathbf{o,n}} + \mathbf{T}_{\mathbf{p,n}} \qquad (8)$$

$\boldsymbol{X_{n+1}}$ is then integrated in time using an explicit time integration scheme to obtain vehicle velocity $\boldsymbol{X_{n+1}}$ and position $\boldsymbol{X_{n+1}}$ at the time step $n + 1$.

Preprints (www.preprints.org) | NOT PEER-REVIEWED | Posted: 26 May 2020 doi:10.20944/preprints202005.0434.v1

3. VALIDATION STUDIES

To correctly study and compare the maneuvering characteristics of an SP-control fin driven UUV and a CP augmented UUV, the CP and 6-DOF maneuvering models were first validated.

3.1 Validation of the Cycloidal Propeller Model

Setup - The framework for CP developed in (Halder and Benedict, 2018) was used to model the CP forces and moments produced in the CP augmented UUV. Wind tunnel experiments were used to test a model CP at a free-stream speed of 3m/s for various CP rotation speeds, results of which were then compared with the predictions of the CP model. Rotor blade pitch amplitude β was set at 45^o (Halder and Benedict, 2018) while the CP phase γ was 90^o.

Table 1: Cycloidal propeller wind tunnel test parameters Halder & Benedict (2018).

Propeller parameters	
Number of Blades	4
Chord	0.665 in
Radius	3 in
Span	6.25 in
Air density	1.225 kg/m^3
Free-stream velocity	3 m/s
Phase angle	90^o
Pitch amplitude	45^o

It must be noted that the rotor blades during the wind tunnel test pitched sinusoidally about their pivots as the rotor disk rotates as governed by Eq. 1. Table 1 lists the model propeller parameters and test parameters used for the validation experiment.

Results - Figure 8 compares CP forces generated during the wind tunnel experiments with those predicted by the CP model, over a wide range of CP rotation speeds, given here in rotations per minute. Since the virtual camber on a rotor blade varies as it moves along the azimuth β, at different β the hydrodynamic forces produced will also be different, resulting in a time varying lift and thrust over 360^o of CP rotation. For this purpose, *time and circumferentially averaged* lift and thrust forces, are used in Figure 8 for the comparison. As can be seen, values predicted by the code matched reasonably well with values measured during the experiments. Hence, this CP model could be used to better understand CP performance characteristics and then be incorporated into the 6 DOF maneuvering model for propulsive load calculations. The only change made for the present work was that the fluid density was changed to that of water.

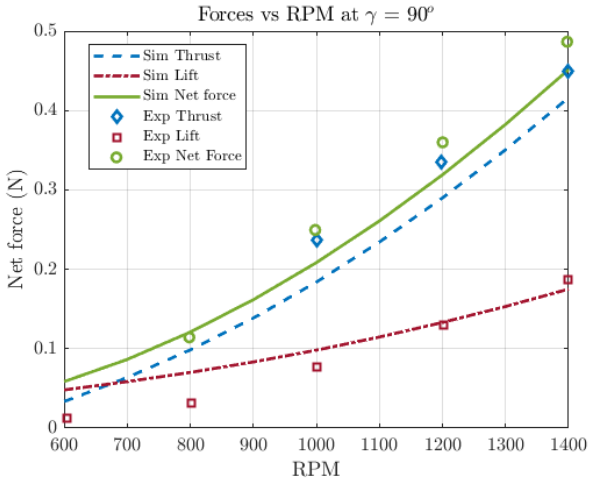

Figure 8: Predicted and measured lift, thrust and net cycloidal propeller force as a function of rotation speed *RPM* at a phase $\gamma = 90^o$. A higher rotation speed understandably generates larger propulsive forces. Data generated from the reduced order CP model (in lines) matches reasonably well with that of the wind tunnel experiments (in markers) (Halder & Benedict, 2018).

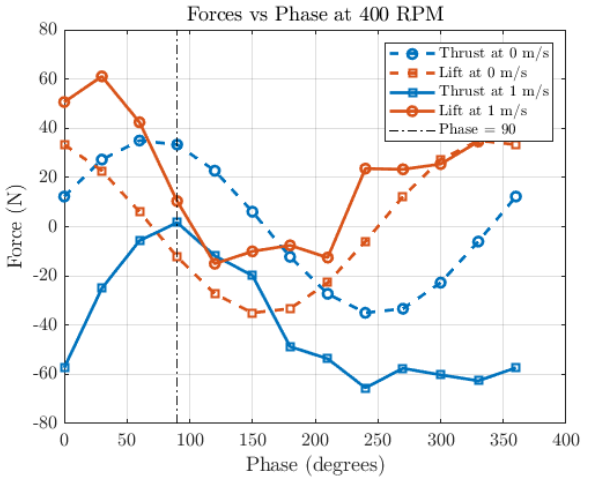

Figure 9: Predicted thrust and lift forces produced by a cycloidal propeller as a function of the phase angle. Free-stream speeds of 0 m/s and 1 m/s are analysed at a cycloidal propeller rotation speed of 400 rpm. As compared to a free-stream at 0 m/s, at the higher free-stream speed of 1 m/s, the cycloidal propeller yielded a higher mean lift, and a lower mean thrust.

Figure 9 shows the variation in lift and thrust forces, as predicted by the CP model, as the phase γ is varied from 0^o to 360^o. For a stationary and purely rotating CP, at 0^o phase, almost the entire hydrodynamic force produced is in the vertically upward direction. As the phase angle is raised towards 90^o, the lift forces

Preprints (www.preprints.org) | NOT PEER-REVIEWED | Posted: 26 May 2020 doi:10.20944/preprints202005.0434.v1

decrease while the thrust force increases, meaning that the direction of the net hydrodynamic force is shifting from the vertically up to the horizontally forward direction.

In a CP that also translates, the rotor blades experience the additional horizontal inflow velocity V_∞. As shown in Figure 5, this produces a differential lift force due to unequal lift forces generated at the top and bottom azimuth rotor blades. As V_∞ increases, so does the mean lift force, while the mean thrust force reduces.

As can be seen in Figure 9, the thrust reduces drastically once the propeller moves in the forward direction since the resultant angle of attack reduces due to increased forward velocity. These results explain why CP tend to experience a decrease in efficiency and increase in power consumption as the forward speed is increased. Hence in Section 4, we explore the concept of, and use CP, to augment the maneuverability of a UUV.

3.2 Validation of 6 DOF Maneuvering Model

The Explorer - The Explorer (Figure 10) is a highly maneuverable and autonomous underwater vehicle (AUV) developed by International Submarine Engineering Ltd ("The Explorer AUV, International Submarine Engineering Ltd.," n.d.). Utilized for defense, academic research and commercial purposes, its chief mission profiles constitute oceanic surveys, environment monitoring and pipeline inspections. The AUV is 4.5 m in length with a maximum diameter of 0.69 m. It is designed to operate at depths up to 6000 m. Thrusted by a twin-blade propeller, it can reach cruise speeds between 0.5 to 2.5 m/s. On a roughly axisymmetric hull, it has a total of six control planes - two dive planes in front to change depth and four stern planes in an 'X' configuration to provide maneuverability in roll, pitch and yaw. Other specifications of interest can be found in Table 2.

In August 2006, the Explorer was used by the Memorial University of Newfoundland (MUN), Canada, for validating a maneuvering code of its own. At the Holyrood harbor, it conducted acceleration - deceleration tests, zig zag tests, turning circle maneuvers and helical maneuvers as part of an elaborate study.

Figure 10: A 2006 Explorer AUV (Issac, 2011).

Being autonomous, the AUV had an on board controller and associated sensors providing data such as speed, location, trajectory, orientation and depth. The control plane deflections and propeller rotation speed were recorded. For each sea trial, a reference path and target speed were provided to the on board controller through a mission planning and supervision software FleetManager (Fle).

Validation against and analysis of these sea trail results had been conducted as doctoral research and have been published in the resulting doctoral thesis (Issac, 2011). The data provided served as a good reference to test and refine our own maneuvering model and code.

Table 2: Explorer AUV specifications. The data provided pertains to the AUV as of August 2006 (Issac, 2011). Present day specifications can be found at ("The Explorer AUV, International Submarine Engineering Ltd.," n.d.).

Explorer AUV specifications	
Vehicle dry mass	630.6 kg
Vehicle wet mass	1432.7 kg
Total displacement	1446.3 kg
Net displacement	13.6 kg
Vehicle length	4.5 m
Vehicle hull diameter	0.69 m
Control plane span	0.36 m
Control plane chord	0.36 m
Propeller diameter	0.65 m
C.G ahead of C.B by	0.003 m
C.G below C.B by	0.017 m

Screw propeller and Control plane model - The Explorer AUV is thrusted by a dual blade screw propeller and maneuvered by six control planes. Since the on-board data acquisition system time logged propeller rotational speeds and AUV speeds, propeller thrust $\boldsymbol{T}$ and reaction torque $\boldsymbol{Q}$ were curve fit as a function of the AUV speed in (Issac, 2011). $\boldsymbol{T}$ and $\boldsymbol{Q}$ act solely in direction $\boldsymbol{l}'$ in the vehicle reference frame and together with any resulting moments $\boldsymbol{M_p} = \boldsymbol{l} \times \boldsymbol{T}$, are incorporated as $\boldsymbol{T_p}$ in Eq. 8. Here $\boldsymbol{l}$ is the thrust line vector in $1'2'3'$. (Issac, 2011) utilized manufacturer provided performance sheets to determine thrust coefficients K_T, torque coefficients K_Q and efficiencies η of the propeller over a range of advance coefficients λ. Using the works of (Burcher and Rydill, 1994), Taylor's wake fraction and AUV thrust deduction coefficient for the Explorer hull and propeller sizes was determined as 0.2 and 0.1 respectively. Using this knowledge along with straight line acceleration - deceleration test results for the AUV, hull drag and control plane drag were plot as a function of AUV speed. An average AUV drag

Preprints (www.preprints.org) | NOT PEER-REVIEWED | Posted: 26 May 2020 doi:10.20944/preprints202005.0434.v1

coefficient of 0.0143 was determined for use in the maneuvering simulations of (Issac, 2011). During the sea-trial tests, the Explorer AUV speed varied between 1 m/s - 2.5 m/s. This yielded an operating Reynolds number of the order of 10^5 for the UUV. (Issac, 2011) also determines that during the tests the screw propeller had an advance coefficient of ~ 0.6-0.7, which gave it an efficiency of ~ 80%.

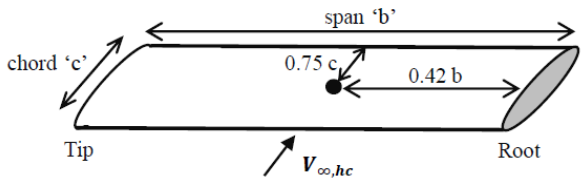

Figure 11: A 2006 Explorer AUV control plane. It had a span and chord of 0.36 m and hence a geometric aspect ratio of 1. However, since the UUV hull connects with the control plane root, its effective aspect ratio was 2.

The control planes are modelled as NACA 0025 hydrofoils. The generated lifts, drags and moments are calculated at the respective hydrodynamic centers *hc* as shown in Eq. 10 - 12 (Issac, 2011). Although the control planes had a geometric aspect ratio of 1, since the UUV hull connects with the control plane root, its effective aspect ratio was taken as 2.

$$\mathbf{V}_{\infty,\mathbf{hc}} = \mathbf{U} + \boldsymbol{\Omega} \times \mathbf{r}_{\mathbf{hc}} \tag{9}$$

$$\mathbf{F}_{\mathbf{fin}} = \begin{bmatrix} D_{fin} \\ L_{fin} \end{bmatrix} = \frac{1}{2}\rho |\mathbf{V}_{\infty,\mathbf{hc}}|^2 S_{fin} \begin{bmatrix} -C_{D,fin} \\ C_{L,fin} \end{bmatrix} \tag{10}$$

$$\mathbf{M}_{\mathbf{fin}} = \mathbf{r}_{\mathbf{hc}} \times \mathbf{F}_{\mathbf{fin}} \tag{11}$$

$\boldsymbol{V}_{\infty,hc}$ is the effective inflow velocity at *hc* due to translational (U) and rotational (Ω) velocities of the AUV. r_{hc} is the position vector of *hc* of the control plane, in the body centered frame *1'2'3*. Planform area S_{fin}, lift $C_{L,fin}$ and drag $C_{D,fin}$ coefficient data for the hydrofoils have been provided in (Issac, 2011). $\boldsymbol{F}_{fin}$ and the resulting moments $\boldsymbol{M}_{fin}$ are transformed into the frame of the vehicle *1'2'3'* and only then incorporated into Eq. 1 as a part of $\boldsymbol{D}_n$. Similar calculations are made for the Explorer hull hydrodynamic forces, and have been explained in detail in (Issac, 2011) and (Evans and Nahon, 2004). Added mass coefficients, vehicle geometry and data necessary for hydrostatic load calculations have all been provided in (Issac, 2011).

Maneuvering tests for validation - Turning Circle Maneuver (TCM) and Horizontal Zig-Zag (HZZ) sea trial tests were chosen for the purpose of validation. TCM is traditionally used to test the rudder effectiveness

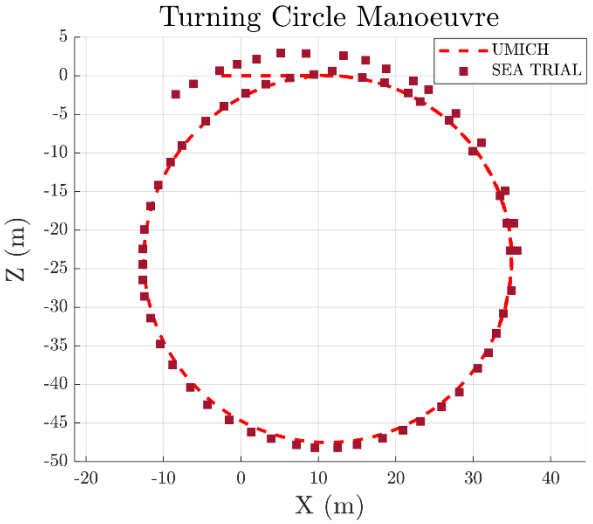

Figure 12: Turning circle maneuver trajectory comparison, using the UUV shown in Figure 10, for a commanded radius R_c = 12 m and a target speed of 1.5 m/s. While the sea trial result was a turn radius of 24.2 m, the maneuvering code predicted a turn radius of 23.9 m.

of sea going vehicles. Such a maneuver is of importance to UUVs since there may be a point of interest which might need to be circled at length for better observation and data collection. HZZ maneuvers traditionally test turning ability of sea vehicles around obstacles. Unlike the Explorer, there was no control system incorporated in our maneuvering code at the time of validation. As a result, only *steady state* portions of the maneuvers were simulated. Time logged control plane deflections, steady state speed and initial vehicle attitudes provided in (Issac, 2011) were given as input in the maneuvering code. The results of our simulation were then compared with those of the sea trials.

The steady state portions of the TCM and HZZ sea trials were performed at a depth of 3 m and speeds of 1.5 m/s and 1 m/s. This yielded a Froude number of ~ 0.28 and ~ 0.18 for the Explorer along with a depth to body diameter ratio of ~ 4.4. This satisfied the requirements to disregard any wave and free surface effects (Faltinsen, 2006). An interesting point to note is that the author of (Issac, 2011) approximates the Explorer *X* tail configuration as a cruciform and calculates the effective control plane deflections to be used in validating his maneuvering code. The author obtained similar results as those in the sea trials and concluded the cruciform approximation of an *X* tail, to be a practical one. This approximation was used in modelling the control planes in the present maneuvering code as well. Therefore, the control plane deflections

Preprints (www.preprints.org) | NOT PEER-REVIEWED | Posted: 26 May 2020 doi:10.20944/preprints202005.0434.v1

used are effectively time averaged deflections for the cruciform tail recorded during the sea trials.

Results

Turning Circle Maneuver test - For a UUV, TCMs are important when circling a point of interest in an exploratory mission or taking a U – turn at the edge of an area being surveyed. For the sea trial, the control system on-board Explorer was given a radius and center coordinate for the circle to be described.

Figure 12 compares the Explorer UUV sea trial trajectory with the corresponding maneuvering code prediction for a commanded turn radius of 12 m. Although a higher turn radius was executed in the sea trial, the author of (Issac, 2011) says improper control system gains on the vehicle might have been a probable cause for the larger turning radius. This does not affect the validation exercise as control surface deflections, chosen by the UUV control system during the sea-trial tests, were used in the simulation. While the sea trial result was a turn radius of 24.2 m, the maneuvering code predicted a turn radius of 23.9 m. The target speed of 1.5 m/s was maintained throughout the duration of the simulation. The difference in radii can be attributed to a neglect of cross–currents in the sea and use of time averaged (and not instantaneous) control plane deflections.

Figure 13 compares the sea trial and code predicted UUV drift and yaw rate angles. Usage of fixed (time averaged) control plane deflections and modelled damping during simulation result in the steady state turning circle maneuvers and a steady drift rate and

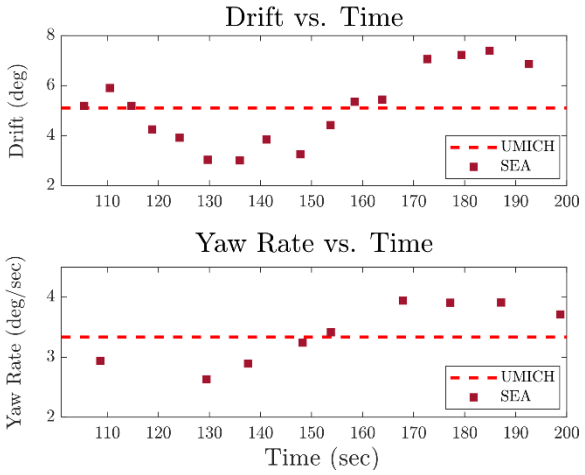

Figure 13: A comparison for the turning circle maneuver steady state yaw rate and UUV drift angles for a commanded radius R_c = 12 m and a target speed of 1.5 m/s, for the UUV shown in Figure 10. In the simulations, control surface deflections, chosen by the UUV control system during the sea-trial tests, were used.

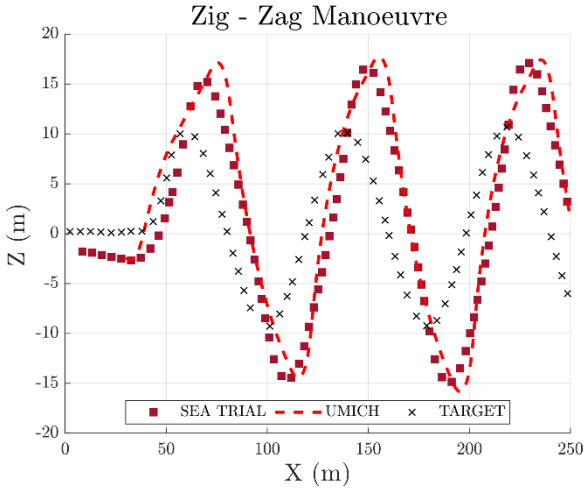

Figure 14: Horizontal zig-zag maneuver comparison at a target speed of 1.5 m/s for the UUV shown in Figure 10. The target sinusoidal path has a wavelength of 80 m and amplitude of 10 m. Waypoints for this sinusoidal reference trajectory were provided at its crests and troughs.

yaw angle. This results in the flat line observed. The control system on-board the Explorer would have constantly changed control plane deflections to counter disturbances and dynamics unmodelled in the simulations, leading to a fluctuating drift rate and yaw angle during the sea trial. Simulations were also conducted for larger turn radii, results of which have been presented in Table 3.

Horizontal Zig - Zag Maneuvere test - For a UUV, an HZZ tests its ability of obstacle avoidance. For the sea trial, the on-board control system was given way-points to refer to a target sinusoidal path. In this case, the crests and troughs of the sine curve were the waypoints. During the sea trial, it was observed that the control system changed (reversed) rudder deflection only when a waypoint was crossed. This is unlike a conventional HZZ maneuver wherein rudder angle of the marine craft is reversed once the target heading is achieved. The resulting time lag in correcting the heading caused an overshoot, as can be seen in Figure 14. At the turns, the controller overcompensated for a drop in speed, by raising the surge speed beyond 1.5 m/s, leading to a further increase in overshoot (Issac, 2011).

Nonetheless, time averaged deflections provided in (Issac, 2011) were used to simulate the maneuver. As can be seen in Figures 12 - 14, a reasonable comparison between the predicted and sea trial measurements was obtained. Differences in simulation predicted and actual

Preprints (www.preprints.org) | NOT PEER-REVIEWED | Posted: 26 May 2020 doi:10.20944/preprints202005.0434.v1

Table 3: Sea trial and simulated turning circle maneuver results for commanded radii R_c = 12 m, 16 m, 20 m, 25 m and 30 m at 1 m/s and 1.5 m/s, for the UUV shown in Figure 10. u is the steady state UUV speed during the sea trial. R is the turning radius executed while θ is the steady state pitch during the turn. r and β are the steady state yaw rate and drift angles. The subscripts s and UM denote the MUN sea-trial and the 6-DOF maneuvering code simulation results respectively.

R_c (m)	u (m/s)	R_s (m)	R_{UM} (m)	β_s (deg)	β_{UM} (deg)	r_s (deg/s)	r_{UM} (deg/s)	θ_s (deg)	θ_{UM} (deg)
12	1.5	24.2	23.9	5.6	5.1	3.5	3.3	-1.6	-1.3
	1.0	23.8	25.5	5.8	4.5	2.4	2.1	-5.0	-9.1
16	1.5	21.5	20.1	2.3	5.9	3.9	4.0	-1.9	-1.8
	1.0	26.6	28.5	5.2	4.0	2.2	2.0	-5.5	-8.8
20	1.5	24.7	24.1	2.0	5.0	3.5	3.4	-1.9	-0.9
	1.0	29.7	32.4	5.2	3.8	2.0	1.9	-5.2	-8.6
25	1.5	28.8	29.3	1.7	4.2	3.0	2.8	-1.9	-0.5
	1.0	29.7	32.4	5.2	3.8	2.0	1.9	-5.2	-8.6
30	1.5	33.3	34.4	1.5	3.7	2.6	2.4	-1.8	-0.4
	1.0	37.5	41.1	3.8	3.0	1.5	1.5	-5.4	-8.9

trajectories can once again be attributed to neglect of cross – currents in the sea and use of time averaged (and not instantaneous) control plane deflections. Since the 6-DOF maneuvering model made reasonably well predictions, it was used along with the CP model to simulate and compare maneuvering characteristics of the SP-control fin driven and CP augmented UUV.

4. CYCLOIDAL PROPELLER VS. SCREW PROPELLERS

4.1 UUV Configuration and Assumptions

Once the cycloidal propeller and 6-DOF maneuvering models were validated, the next step was to compare the maneuvering performances of an SP and fin driven UUV with that of a CP augmented UUV. We opted to explore the performance of a CP augmented UUV as CP alone would lead to poor performance (high propulsion power requirements) at high UUV design speeds, as already explained in Section 3.1. While conceptualizing the CP augmented UUV, few simplifying assumptions were made which have been explained next.

1. In the CP augmented UUV, there will be no dive planes. Dive planes primarily serve to alter UUV depth, a function now to be performed by the CP.

2. In all, four CP will be placed symmetrically on the UUV, in an arrangement shown in Figure

3. Two CP will be located a meter forward and a meter aft of the center of buoyancy (CB). All four CP will lie in the horizontal plane containing the CB.

4. It is also assumed that in both cases the center of gravity (CG) will coincide with the CB in the horizontal plane and only have a vertical separation (same as that in the Explorer).

5. The UUVs will be neutrally buoyant.

6. Presence of CP will not affect the flow and hence the performance of either the stern planes or the screw propeller in the CP augmented UUV.

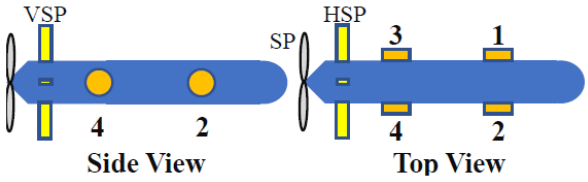

Figure 15: A simplified diagram of the cycloidal propeller augmented Explorer UUV. The dive planes have been removed. HSP are the horizontal stern planes (elevators) while VSP are vertical stern planes (rudder). SP is the twin blade screw propeller on the Explorer UUV.

Preprints (www.preprints.org) | NOT PEER-REVIEWED | Posted: 26 May 2020 doi:10.20944/preprints202005.0434.v1

7. Additional inertia and buoyancy of the CP are assumed to be much smaller than that of the UUV and are therefore ignored.

8. The UUVs will operate at low speeds in open water, hence the cycloidal propeller blades are assumed to not cavitate, ventilate or bend under hydrodynamic loads. Also, responses of the CP and control plane deflections to a command are assumed to be instantaneous, i.e, there is *no time lag*.

To re-iterate, at higher speeds the screw propeller will provide the necessary thrust while the stern planes will maneuver the vehicle and the rudder will remain undeflected; the CP can be used to augment the thrust and maneuverability at high speeds. At low speeds, the CP will provide all the necessary thrust *and* maneuvering forces.

4.2 Sizing the Cycloidal Propellers

Similar to how SP are sized based on thrust requirements, it was necessary to generate thrust-speed characteristic curves for the CP and select an efficient operating point. CP designed in the Advanced Vertical Flight Laboratory at Texas A&M University (TAMU) were used as a baseline (Figure 1). Dimensions of this baseline CP are shown below in Table 4.

Table 4: The baseline cycloidal propeller parameters.

Propeller parameters	
Number of Blades	4
Chord	2 in
Radius	3 in
Span	5 in
Blade section	NACA 0009

The Explorer hull had a diameter of ~ 28 inches and control planes had a span of ~ 14 inches. It was assumed that the CP fit onto them can have a rotor disk of half the hull diameter and a blade of span half that of the control plane. The rotor blade chord was kept the same as that in the baseline. Dimensions of this model CP are shown in Table 5. In this model CP, the geometric blade aspect ratio increased to 3.5 from 2.5 and the blade chord c over rotor disk radius R ratio was reduced to 0.29 from 0.66. Based on our discussion in Section 2.1, a lower c/R ratio is good for thrust production and lowering CP power requirements. An increased aspect ratio (assuming that the blades do not are made of stiff material and will have negligible deformation) will help increase hydrodynamic efficiency of the blades and hence the operational efficiency of the CP.

Table 5: The model cycloidal propeller parameters for the comparison tests.

Propeller parameters	
Number of Blades	4
Chord	2 in
Radius	7 in
Span	7 in
Blade section	NACA 0009

To generate the performance curves of this CP, operating parameters were selected as follows. Rotor blade pitch amplitude θ_{amp} was set as 45^o for the first half time period and 35^o for the second half time period of CP rotation, since this combination was found to be more effective (Benedict et al., 2013) than a uniform blade pitch amplitude in reducing the transverse forces generated by CP (Section 2.1). The CP phase γ was set to 96^o, the angle at which most of the hydrodynamic force produced is in the thrust direction for the given dimensions and operating parameters of the CP. Also, as the rotor moves, the rotor blade pitch angle was chosen to vary *cycloidally* about its pitch axis as this yielded better operating efficiencies than pitching the blades sinusoidally. The eccentricity e was set as 0.48. The number of blades N_b were chosen to remain as four since it provided superior power loading over the blade pitch amplitude range of 25^o to 45^o (Benedict et al., 2010). Also, the lift slope C_{l_α} of the rotor blades was calculated as in (Kerwin et al., 2010)

$$C_{l_\alpha} = \frac{2\pi}{1+\left(\frac{2\pi}{2\times AR}\right)} \tag{12}$$

Performance curves were generated for an advance coefficient $J \in (0,1)$ and a UUV surge speed (and hence CP free-stream speed) of 0.5 m/s. Although the UUV speed will not affect the performance curves of the vehicle, a low speed was chosen since the goal of this paper is to show the potential advantages of a CP augmented UUV at low UUV speeds. Eq. 14 - 16 define the non-dimensional time-averaged quantities (Turbo, n.d.) used to generate the characteristic curves for the model CP.

$$K_T = \frac{Thrust}{\frac{1}{2}\rho d b u^2} \tag{13}$$

Preprints (www.preprints.org) | NOT PEER-REVIEWED | Posted: 26 May 2020 doi:10.20944/preprints202005.0434.v1

$$K_Q = \frac{Torque}{\frac{1}{4}\rho d b u^2} \tag{14}$$

$$\eta = \lambda\left(\frac{K_T}{K_Q}\right) \tag{15}$$

K_T, K_Q and η are the CP thrust coefficient, torque coefficient and efficiency respectively. *Thrust* and *Torque* are the CP produced thrust and torque. n is the CP speed in rotations per second. d and b are the CP diameter and blade span respectively. $\lambda = V_a/(\pi n d)$ is the advance coefficient for the CP while $u = \pi n d$ is the peripheral speed of the blades. V_a is the reference UUV surge speed (and hence also the freestream flow speed into the CP).

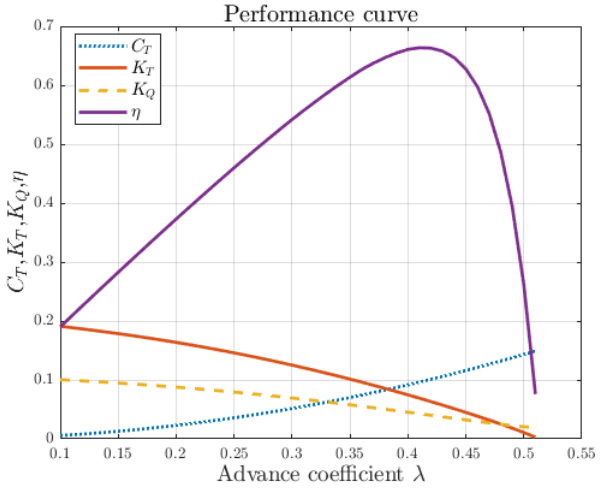

Figure 16: Model cycloidal propeller performance curves.

Figure 16 shows the CP characteristic curves obtained. We see that the CP has a maximum efficiency of ~ 66% at an advance coefficient of $\lambda \sim 0.42$. To determine the operating point, a *required* thrust coefficient C_T was calculated as follows,

$$C_T = \frac{0.25 \times Drag}{\frac{1}{2}\rho d b u^2} \tag{16}$$

Drag C_T is the non-dimensionalized drag which must be overcome by a *single* cycloidal propeller (hence the *0.25* multiplier). In Figure 16 we see that the K_T and C_T lines intersect at $\lambda = 0.38$ and $\eta \sim 0.65$. This is the design point of the model cycloidal propeller. Since K_T and C_T are non-dimensional numbers, for the given CP dimensions and operating parameters (θ_{amp}, γ, e, N_b, $C_{l\alpha}$) the design point will remain unchanged irrespective of V_a and n. Although we obtain an η of only 65%, as compared to 80% with the screw propeller on the Explorer UUV, we must keep in mind that the CP is not yet fully optimized. Blade section and blade planform can be further improved and along with use of stronger fabrication materials, more efficient CP blades and CP can be made. Since the paper aims to show the potential advantage of a CP augmented UUV in providing swift maneuvering in added DOF, we move forward with this model CP configuration, even though it offers a lower efficiency.

4.3 Turning Circle Maneuver at 1.5 m/s

The objective of the TCM comparison is to show that a CP augmented UUV can execute turns similar to those of an SP-control fin driven UUV, even when solely thrusted and maneuvered by CP.

Figure 17 compares the TCM trajectories of the SP-control fin UUV during sea trial and CP augmented UUV in the simulation. The sea trial maneuver is the same as the one used earlier in Section 3, but is now on the port side. $\delta Y = 5.9^o$ and $\delta Y = 7.5^o$ are two cases wherein the CP only provides the thrust necessary to maintain a steady surge speed of 1.5 m/s, while the rudder provides the steering moments to execute the turn. As can be seen, a larger fin deflection has produced a sharper turn and reduced turning radius. $\delta Y = 0^o$ is the case where the CP augmented UUV describes a circle similar to that in the sea trial. Here, the rudder is undeflected and the CP *additionally* provides steering

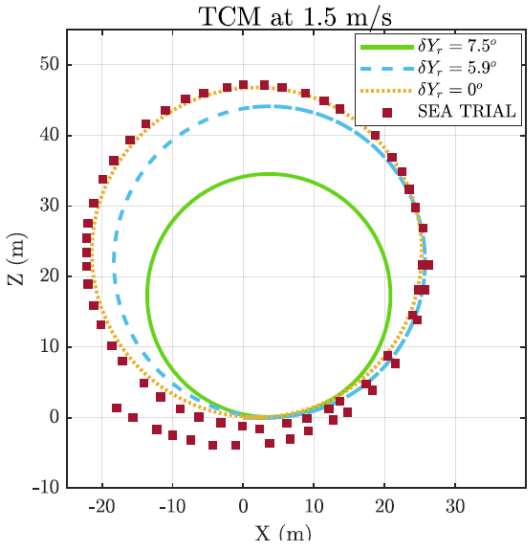

Figure 17: Turning circle maneuver comparison at a target speed of 1.5 m/s in port direction. The $\delta Y = 7.5^o$ and $\delta Y = 5.9^o$ cases have the cycloidal propellers provide only thrust, while the rudders provide the steering moments. In the $\delta Y = 0^o$ case, the rudder is undeflected and the cycloidal propellers provide thrust *and* steering moments.

Preprints (www.preprints.org) | NOT PEER-REVIEWED | Posted: 26 May 2020 doi:10.20944/preprints202005.0434.v1

moments for the TCM. As can be seen in Table 6, this comes at the cost of an appreciably higher power. The steering moments require higher CP RPM, leading to a larger power draw. For this test case, the CP rotation speed and phase were selected in a way that provided the same thrust and turn initiating moment as in the SP-control fin case (sea trial). Since the UUV must yaw to one side, RPM of CP on one side must be larger than that on the other side to produce a thrust differential and turning moment. In this simulation, CP 2 and CP 4 were driven at a high RPM to provide a high positive thrust, while CP 1 and CP 3 were driven at a low RPM to generate a negative thrust. Such a strategy allowed us to achieve the required thrust (difference of thrust from CP 2,4 and CP 1,3), while also creating a sufficiently strong turning moment (sum of individual CP turning moments) to steer the UUV. Diagonally opposite CP (CP 2,3 and CP 1,4) were rotated in opposite directions so as to minimize the net lift force produced.

Table 6: Turning circle maneuver comparison at a target speed of 1.5 m/s. Cycloidal propeller $\mathcal{CP}$ rotation speed $\mathcal{N}$ and corresponding phase ϕ required to execute the maneuvers are listed along with the steady state turn radius R_S. R_S in the sea trial was 24.2 m. $\mathcal{P}$ lists the total power to be provided to the propellers.

Case	CP	N (rpm)	γ (deg)	R_S (m)	P (W)
$\delta Y = 7.5^o$	1-4	196	97	17	4 x 80
$\delta Y = 5.9^o$	1-4	196	97	22	4 x 80
$\delta Y = 0^o$	2,4 1,3	310 65	96 295	23	2 x 535 2 x 36

4.4 U-turn at 0.1 m/s

A U-turn at 0.1 m/s is a low speed maneuvers a UUV will find useful when performing inspection like tasks in restricted waters or when wanting to circle a point of interest for extended imaging and data collection. For this comparison, rudder deflection in the SP-control fin driven UUV was set to 30^o. In the CP augmented UUV, CP rotation speed and phase were selected for two turning rates r, a high yaw rate of 10 deg/sec and a lower yaw rate of 5 deg/sec. The rudders once again remained undeflected.

Figure 18 compares the trajectories for the three cases. The grey elliptical patch represents the starting point for the UUV in each case. In blue is the SP-control fin UUV while in green is the CP augmented UUV. We see that with SP, the UUV executes a turn occupying a much larger area as compared to when maneuvered using CP. As can be seen in Table 7, its

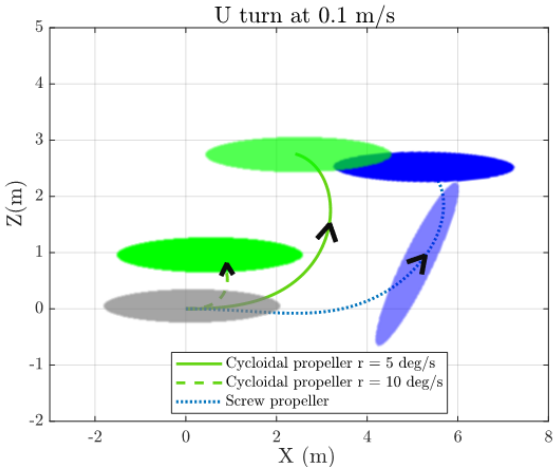

Figure 18: 180^o turn comparison for the cycloidal propeller augmented and screw propeller-control fin driven UUV for a target speed of 0.1 m/s. In each case shown above, the UUV turns at high drift angles. This is shown only for the screw propeller case for sake of clarity. The grey ellipsoid represents the starting position for all the UUVs.

response time of 95 seconds (r = 1 deg/s) is a lot more sluggish as compared to the 18 seconds (r = 10 deg/s) with the CP. This is due to the fact that at low speeds, such as 0.1 m/s, the fin steering forces ($\propto$ speed^2) are too low to allow a swift response to a rudder deflection as large as 30^o. On the other hand, CP maneuvering forces being much less dependent on UUV speed, continue to provide effective steering moments to the UUV, leading to a quicker and more compact response. Quite naturally, higher turning rates

Table 7: 180^o turn comparison for a target speed of 0.1 m/s. Cycloidal propeller rotation speed $\mathcal{N}$ and corresponding phase γ required for the cycloidal propellers $\mathcal{CP}$ to execute the maneuvers are listed along with the time t_U taken. $\mathcal{P}$ lists the total power to be provided to the propellers. $\mathcal{E}$ lists the estimated energy consumed by the cycloidal propellers while the maneuver is executed.

r (^{o}/s)	CP	N (rpm)	γ (deg)	t_U (s)	P (W)	E (W-h)
10	2,4 1,3	165 150	97 278	18	2x110 2x87	2x0.55 2x0.44
5	2,4 1,3	87 25	97 250	47	2x10.5 2x2	2x0.06 2x0.01

Preprints (www.preprints.org) | NOT PEER-REVIEWED | Posted: 26 May 2020 doi:10.20944/preprints202005.0434.v1

will require higher CP rotation speeds and power draw. Since the UUV must yaw to one side, RPM of CP on one side must be larger than that on the other side to produce a thrust differential and turning moment. A strategy similar to that in the turning circle maneuver was used to simulate this U-turn. Diagonally opposite CP were once again rotated in opposite directions to minimize the net lift force produced.

4.5 Heave at 0.5 m/s

When approaching or operating near the seabed, UUVs must execute a controlled heave motion. Some UUVs have tunnel thrusters meant only for this purpose, and are redundant otherwise. UUVs without additional thrusters, like the Explorer, utilize control planes (elevator or dive planes) to gain height or depth. They do so by pitching up or down and moving along a curved trajectory, i.e, alter *depth by heave* (Issac, 2011). Being maneuvered by control planes, the UUV must have a finite surge velocity for the control planes to be effective. As a result, while heaving, the UUV will also advance in surge. This may not always be feasible, especially when descending narrow passages.

Figure 19 shows a comparison between heave trajectories for a SP-control fin steered UUV and CP augmented UUV. The grey elliptical patch represents the starting point for the UUV in each case. Motion between depths of 7 m and 10 m is analysed. The SP driven UUV (in blue) moves at 1.5 m/s and pitches by ~ -6^o to gain depth. Time logged positions and pitch angles recorded in (Issac, 2011) were used to recreate the UUV motion. The UUV took 10 seconds to descend the 3 m depth and advanced close to 15 m in surge in the process. On the other hand, the CP augmented UUV (in green) is capable of descending straight down, simply by vectoring thrust in the downward direction. Moving at 0.5 m/s, it takes 6 seconds to move to the 10 m depth. More importantly, it does not advance significantly in surge.

Table 8: Heave comparison at 0.5 m/s. Cycloidal propeller rotation speed N and corresponding phase γ required for the scaled cycloidal propellers to execute the maneuver are listed. P lists the total power to be provided to the propellers. E lists the estimated energy consumed by the cycloidal propellers while the maneuver is executed.

CP	N (rpm)	γ *(deg)*	P (W)	E (W-h)
1, 2	243	96	2x 329	2x 0.55
3, 4	183	96	2x 134	2x 0.22

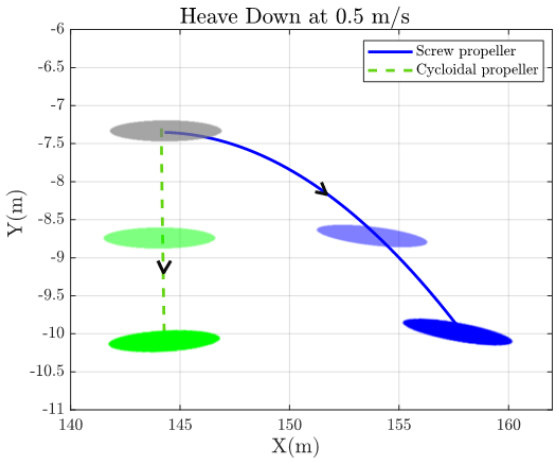

Figure 19: Heave trajectory comparison at a target speed of 0.5 m/s for the cycloidal propeller augmented and screw propeller-control fin driven UUVs. With the screw propeller control fin combination, the UUV travels a significant distance in surge as it heaves down.

The CP rotation speeds and phase were selected in a manner that yielded thrust sufficient to maintain a speed of 0.5 m/s in heave, and a pitching moment close to zero. As can be seen in Figure 19, perfect trim is not attained and the UUV pitches up to 5^o, pointing towards the need of a control system for carrying out such maneuvers.

5. CONCLUSION AND FUTURE WORK

The present work investigated the novel concept of a cycloidal propeller augmented UUV. Simulations were used to demonstrate the potential of cycloidal propellers in enhancing the maneuverability of a UUV, especially at low speeds. Cycloidal propellers are envisioned to thrust and maneuver the vehicle at low UUV speed while the screw propeller-control fin combination will provide majority of the thrust and maneuvering at higher UUV speeds. To this end, a low speed U-turn was simulated to show the capability of a cycloidal propeller to provide a more compact and quicker response, at a speed as low as 0.1 m/s. Such a low speed could be encountered at the time of underwater inspection, station-keeping or dynamic positioning like tasks.

Next, a low speed heave maneuver was used to show the capability of cycloidal propellers to provide added maneuverability in the heave degree of freedom. Unlike the screw propeller-fin combination, cycloidal propellers allowed the UUV to descend straight down without advancing in surge and occupying space, especially critical when operating in restricted waters. All maneuvering simulations were carried out using validated cycloidal propeller (Halder and Benedict, 2018) and maneuvering models. The 6-DOF

maneuvering model and code developed in-house will henceforth provide a computationally cheaper alternative to study maneuvering characteristics of sea going vehicles.

The cycloidal propellers used in the simulations had relatively low operational efficiencies, unlike commercial cycloidal propellers such as the Voith Schneider propellers (with reported efficiencies as high as 80%) found on ships. The low efficiency can be attributed to the blade section and blade planform being sub-optimal. Absence of end plates also add to a reduced efficiency. Further investigation and optimization of such parameters can help enhance propeller performance. Additionally, rotor blade material optimization and reinforcements to account for the large hydrodynamic loads in water will allow use of higher aspect ratio blades. Another interesting point to note was the estimated duration and energy consumption of the simulated maneuvers. Although the power draw was of the order of 0.1 kW for the low speed simulations, energy consumed was only of the order of 10^{-3} kWh, which is much lower than the battery capacities (order of~10 kWh) of present day UUVs. Also, depending on the application, the UUV may spend a larger portion of the mission duration in getting to the point of interest. During this time, the screw propellers and fins can be used to ensure efficient and fast travel. A relatively shorter duration may be spent while surveying and/or collecting the data, during which time the cycloidal propellers can be used for accurate positioning and swift maneuvering. Therefore, based on the mission profile for the UUV and the actuators on-board, a trade-off can be made for enhanced and compact maneuverability in added degrees of freedom, over a low operational efficiency for a short duration of time.

Lastly, the present study simulated the UUV only in open water conditions. Waves, currents and complex fluid phenomena like cavitation and ventilation were ignored. It is essential to include them in future simulation studies, especially while designing controllers for a cycloidal propeller augmented UUV or amphibious vehicle that needs to operate at higher speeds or near the surface. Underwater currents will act like disturbances while waves will introduce wave drag and frequency dependence in fluid-added mass and damping of the vehicle. Cavitation and ventilation may occur on fast moving rotor blades, especially when operating close to the surface. Generally speaking, cavitation occurs when the local pressure of water reduces to a value below its saturation pressure, leading to its vaporization in this low pressure region. Cavitation is a common cause for concern in hydraulic turbine and screw propeller blade tips. On the other hand, ventilation occurs when air from over the free surface gets sucked down by the low pressure regions of the rotor blade. Ventilation is a common occurrence in surface piercing hydrofoils on boats. Both cavitation and ventilation can lead to large and sudden drops in lift/thrust, and cause vibration and noise in both screw and cycloidal propellers. It is therefore necessary to predict the onset of such phenomena and mitigate their effects by pre-emptively altering propeller operating parameters like rotation speed and phase.

Hence, future work involves incorporating the associated physics of cavitation and ventilation in the reduced order hydrodynamic model developed by (Halder and Benedict, 2018). On the maneuvering side, wave and currents will be modeled into the six DOF maneuvering code. Both these steps will allow sea vehicle simulations in more realistic environments and aid development of a control system for the cycloidal propellers in the cycloidal propeller augmented UUV.

ACKNOWLEDGEMENTS

The authors are grateful for the funding provided for this study by the Office of Naval Research (ONR) grant no. N00014-18-S-B001 managed by Troy Hendricks.

REFERENCES

Benedict, M., Jarugumilli, T., Chopra, I., 2013. Effect of rotor geometry and blade kinematics on cycloidal rotor hover performance. Journal of Aircraft 50, 1340–1352.

Benedict, M., Jarugumilli, T., Lakshminarayan, V., Chopra, I., 2014. Effect of flow curvature on forward flight performance of a micro-air-vehicle-scale cycloidal-rotor. AIAA journal 52, 1159–1169.

Benedict, M., Ramasamy, M., Chopra, I., 2010. Improving the aerodynamic performance of micro-air-vehicle-scale cycloidal rotor: an experimental approach. Journal of aircraft 47, 1117–1125.

Brennen, C.E., 1982. A Review of Added Mass and Fluid Inertial Forces.

Burcher, R., Rydill, L., 1994. Concepts in underwater vehicle design.

Evans, J., Nahon, M., 2004. Dynamics modeling and performance evaluation of an autonomous underwater vehicle. Ocean Engineering 31, 1835–1858.

Faltinsen, O.M., 2006. Hydrodynamics of High-Speed Marine Vehicles by Odd M. Faltinsen.

Fossen, T.I., 2011. Handbook of marine craft hydrodynamics and motion control. John Wiley & Sons.

Griffiths, G., 2002. Technology and applications of autonomous underwater vehicles. CRC Press.

Halder, A., Benedict, M., 2018. Nonlinear Aeroelastic Modeling of Cycloidal Rotor in Forward Flight. AHS Technical Meeting on Aeromechanics Design for Transformative Vertical Lift, San Francisco, California, January 20-22, 2018.

Halder, A. Moble, B., 2018. Nonlinear Aeroelastic Modeling of Cycloidal Rotor in Forward Flight, in: AHS Technical Meeting on Aeromechanics Design for Transformative Vertical Lift.

Halder, A., Walther, C., Research, G., Benedict, A.M., 2017. Unsteady Hydrodynamic Modeling of a Cycloidal Propeller.

Hibbeler, R.C., Yap, K.B., 2012. Mechanics for Engineers: Dynamics. Pearson Education South Asia Pte Ltd.

Issac, M.T., 2011. Analysis of full-scale sea-trials maneuvering data and development and validation of a motion-simulation model for the AUV MUN Explorer.

Kerwin, J.E., Hadler, J.B., Paulling, J.R., 2010. Propulsion. Society of Naval Architects and Marine Engineers.

Newman, J.N., 2018. Marine hydrodynamics. MIT press.

Nicholson, J.W., Healey, A.J., 2008. The present state of autonomous underwater vehicle (AUV) applications and technologies. Marine Technology Society Journal 42, 44–51.

Shen, Y., Fuhs, D., 1997. Blade section lift coefficients for propellers at extreme off-design conditions.

The Explorer AUV, International Submarine Engineering Ltd., n.d.

Turbo, V., n.d. The Voith Schneider Propeller Current Applications and New Developments.

APPENDIX

A. Rotation matrices

ψ , ϕ and θ are the Euler angles of orientation of 1'2'3' in the inertial coordinate system 123. Eq. A.1 and A.2 show the effective rotation matrix R (Fossen, 2011) that orients $\vec{x}$ - a vector in the vehicle frame 1'2'3' to $\vec{X}$ - a vector in the inertial frame 123.

$$R = \begin{bmatrix} c\psi c\theta & -s\psi c\phi + c\psi s\theta s\phi & s\psi s\phi + c\psi c\phi s\theta \\ s\psi c\theta & c\psi c\phi + s\phi s\theta s\psi & -c\psi s\theta + s\psi s\theta c\phi \\ -s\theta & c\theta s\phi & c\theta c\phi \end{bmatrix} \quad (17)$$

where c. = cos(.) and s. = sin(.) and $X_i = R_{ij} x_j$; $i, j = 1, 2, 3$.

B. Equation of Motion matrices

Eq. B.1 - B.11 list the expansions for the matrices used in the 6-DOF equations of motion.

Structural mass matrix $\boldsymbol{M_S}$

$$\mathbf{M_S} = \begin{bmatrix} mI_{3x3} & -mS(r_g^b) \\ mS(r_g^b) & mI_b \end{bmatrix} \quad (18)$$

m is the wet mass of the vehicle. I_{3x3} is the identity matrix while I_b is the vehicle rotational inertia matrix in the body fixed frame 1'2'3 defined as,

$$I_b = \begin{bmatrix} I_{1'1'} & -I_{1'2'} & -I_{1'3'} \\ -I_{2'1'} & I_{2'2'} & -I_{2'3'} \\ -I_{3'1'} & -I_{3'2'} & I_{3'3'} \end{bmatrix} \quad (19)$$

r^b_g is the position vector, in the body fixed frame 1'2'3', of the point about which moments are evaluated. This is usually the center of gravity of the vehicle. S is defined as follows for $\boldsymbol{k} = [k_1, k_2, k_3]$,

$$S(\mathbf{k}) = \begin{bmatrix} 0 & -k_3 & k_2 \\ k_3 & 0 & -k_1 \\ -k_2 & k_1 & 0 \end{bmatrix} \quad (20)$$

Fluid added mass matrix $\boldsymbol{M_A}$

$$\mathbf{M_{A_{ij}}} = \left(X_i\right)_{\dot{v}_j} \quad (21)$$

$\left(X_i\right)_{\dot{v}_j} = \dfrac{\partial X_i}{\partial \dot{v}_j}$ is the hydrodynamic derivative for the fluid added mass as per SNAME conventions. v is the acceleration vector of the vehicle in the body fixed

Preprints (www.preprints.org) | NOT PEER-REVIEWED | Posted: 26 May 2020 doi:10.20944/preprints202005.0434.v1

frame 1′2′3′. i, j = 1, 2, 3 for translational and i, j = 4, 5, 6 for rotation along axes 1′,2′ and 3′.

Structural Coriolis-centripetal matrix $\boldsymbol{C_S}$

$$\mathbf{C_S} = \begin{bmatrix} 0_{3x3} & -S(M_{11}v_1 + M_{12}v_2) \\ -S(M_{11}v_1 + M_{12}v_2) & -S(M_{21}v_1 + M_{22}v_2) \end{bmatrix} \quad (22)$$

$v_1 = [u, v, w]^T$ and $v_2 = [p, r, q]^T$. Here, M_S has been split into four 3x3 sub-matrices,

$$\mathbf{M_S} = \begin{bmatrix} M_{11} & M_{12} \\ M_{21} & M_{22} \end{bmatrix} \quad (23)$$

Fluid Coriolis-centripetal matrix $\boldsymbol{C_A}$

$$\mathbf{C_A} = \begin{bmatrix} 0_{3x3} & -S(A_{11}v_1 + A_{12}v_2) \\ -S(A_{11}v_1 + A_{12}v_2) & -S(A_{21}v_1 + A_{22}v_2) \end{bmatrix} \quad (24)$$

Here, M_A has been split into four 3x3 sub-matrices,

$$\mathbf{M_A} = \begin{bmatrix} A_{11} & A_{12} \\ A_{21} & A_{22} \end{bmatrix} \quad (25)$$

Non-linear damping matrix $\boldsymbol{D_{nl}}$

$$\mathbf{D_{nl_{ij}}} = (X_i)_{v_j|v_j|} \quad (26)$$

$(X_i)_{v_j|v_j|} = \dfrac{\partial X_i}{\partial(v_j \,|\, v_j \,|)}$ is the hydrodynamic derivative for the non-linear damping forces and moments as per SNAME conventions. i, j = 1, 2, 3 for translational and i, j = 4, 5, 6 for rotation along axes 1′,2′ and 3′.

Linear damping matrix $\boldsymbol{D_l}$

$$\mathbf{D_{l_{ij}}} = (X_i)_{v_j} \quad (27)$$

$(X_i)_{v_j} = \dfrac{\partial X_i}{\partial v_j}$ is the hydrodynamic derivative for the linear damping forces and moments as per SNAME conventions. i, j = 1, 2, 3 for translational and i, j = 4, 5, 6 for rotation along axes 1′,2′ and 3′.

Hydrostatic forces and moments $\boldsymbol{g_i}$

$$\mathbf{g_i} = \begin{bmatrix} (W-B)sin\theta \\ -(W-B)sin\phi cos\theta \\ -(W-B)cos\phi cos\theta \\ -(Wx_3^G - Bx_3^B)cos\phi cos\theta - (Wx_2^G - Bx_2^B)sin\phi cos\theta \\ -(Wx_2^G - Bx_2^B)sin\theta + (Wx_1^G - Bx_1^B)cos\phi cos\theta \\ -(Wx_1^G - Bx_1^B)sin\phi cos\theta - (Wx_3^G - Bx_3^B)sin\theta \end{bmatrix} \quad (28)$$

W is the self-weight of the vehicle while B is the buoyancy force acting on the vehicle. x^B and x^G pertains to the center of buoyancy and center of gravity coordinates respectively, while θ and ϕ are the pitch and roll angles respectively.